

# Interfacial resistive switching by multiphase polarization in ion-intercalation nanofilms

Huanhuan Tian<sup>†</sup> and Martin Z. Bazant<sup>\*,†,‡</sup>

<sup>†</sup>*Department of Chemical Engineering, Massachusetts Institute of Technology, Cambridge, MA 02139, USA*

<sup>‡</sup>*Department of Mathematics, Massachusetts Institute of Technology, Cambridge, MA 02139, USA*

E-mail: bazant@mit.edu

## Abstract

Nonvolatile resistive-switching (RS) memories promise to revolutionize hardware architectures with in-memory computing. Recently, ion-intercalation materials have attracted increasing attention as potential RS materials for their ion-modulated electronic conductivity. In this Letter, we propose RS by multiphase polarization (MP) of ion-intercalated thin films between ion-blocking electrodes, in which interfacial phase separation triggered by an applied voltage switches the electron-transfer resistance. We develop an electrochemical phase-field model for simulations of coupled ion-electron transport and ion-modulated electron-transfer rates and use it to analyze the MP switching current and time, resistance ratio, and current-voltage response. The model is able to reproduce the complex cyclic voltammograms of lithium titanate (LTO) memristors, which cannot be explained by existing models based on bulk dielectric breakdown. The theory predicts the achievable switching speeds for multiphase ion-intercalation materials and could be used to guide the design of high-performance MP-based RS memories.

**keywords:** resistive switching, phase-field modeling, electron transfer, ion intercalation

In the era of Big Data, the transfer of data between the processing unit and memory has increasingly limited the performance of traditional computing architectures. The "von Neumann bottleneck" can potentially be addressed by in-memory computing, which requires resistive-switching (RS) devices with multiple, nonvolatile resistance states that can be tuned by applied voltages.<sup>1-6</sup> RS devices include two-terminal memristors and three-terminal synaptic transistors.<sup>5</sup> The switching can be bipolar or unipolar, depending on whether or not the set and reset voltages require different signs, respectively.<sup>4</sup> Studied RS mechanisms include ion migration,<sup>1,3,7-11</sup> amorphous-crystalline transition,<sup>3,10-13</sup> ferroelectricity,<sup>3,10</sup> and tunneling magneto-resistance.<sup>3,10</sup> This work describes an RS mechanism based on interfacial phase separation that is limited by bulk ion migration.

Typically, the ion migration mechanism incorporates an ion-conducting nanofilm, and an active electrode that can inject (consume) active ions or vacancies into (from) the nanofilm. Specifically, the mechanism is called electrochemical metallization (ECM) if metal cations (e.g.,  $\text{Cu}^{2+}$ ,  $\text{Ag}^+$ ) are active and valence change mechanism (VCM) if oxygen vacancies are active.<sup>1,5</sup> The ion migration mechanism can be further divided into the bulk and interfacial types, according to which resistance dominates. The bulk mechanisms often involve the formation of conductive filaments (e.g., Cu, Ag, or oxygen vacancy rich regions) by implantation of ions or vacancies from an active electrode, and the dissolution of the filaments by a reverse process driven by a reverse voltage (bipolar switching) or by Joule heating generated by a larger voltage (unipolar switching).<sup>8-11,14</sup> In the interfacial mechanisms, usually the two electrodes have, respectively, Ohmic contact and Schottky contact with the nanofilm, and the latter is sensitive to the local concentration of ions or vacancies which can be enriched or depleted by electric field (bipolar switching).<sup>7,11,15-18</sup>

In recent years, ion-intercalation materials, which have been widely used for batteries,<sup>19-21</sup> have received increasing attention as novel ion-migration-based RS materials. These materials allow for reversible insertion of ions into the lattice without destroying the original crystal structure,<sup>22</sup> often following a multi-phase mechanism.<sup>23</sup> Their electronic conductivity usually

depends on ion concentration, since the inserted/deserted ions usually contribute (nearly) free electrons/holes to the conduction/valence bands.<sup>24–28</sup> This property has been directly used to design bulk-type memristors<sup>29</sup> and synaptic transistors<sup>26,30–32</sup> whose ion concentration is adjusted by ion insertion/desertion through the active or gate electrodes. Compared to ECM or VCM devices, such devices should have good reproducibility and controllability since the conductivity can be precisely and reversibly controlled by current pulses.<sup>26</sup>

This work focuses on ion-intercalation memristors enclosed by ion-blocking electrodes, inspired by the LTO (lithium titanate,  $\text{Li}_{4+3\xi}\text{Ti}_5\text{O}_{12}$ ) memristors developed in Ref. 33. LTO is a commonly used anode material for Li-ion batteries, and follows a two-phase mechanism and insulator-metal transition during lithiation ( $\xi : 0 \rightarrow 1$ ).<sup>34</sup> The memristors were made of LTO4 ( $\xi \approx 0$ ) or LTO7 nanofilms ( $\xi \approx 1$ ) sandwiched by Pt electrodes, and showed bipolar switching behaviors. The ion-blocking electrodes make the RS mechanism different from those reviewed before. Refs. 33,35 explain the RS of LTO memristors by the formation of conductive filaments by dielectric breakdown, based on a phase-field model including the electrostatic self-energy that depends on the magnitude of the applied potential. However, the RS predicted by this model is either volatile or irreversible, since the filaments should quickly dissolve after removing the voltage, or never dissolve even with a reverse voltage (see the Supporting Information (SI)).

In this Letter, we propose a new nonvolatile and reversible interfacial RS mechanism, multiphase polarization (MP), for LTO memristors and other similar systems made of multiphase, ion-intercalation nanofilms enclosed by ion-blocking electrodes.

**Mechanism.** We begin by noting the following properties of LTO memristors derived from experimental data: (1) interfacial ET should dominate the total resistance, since the effective conductivity of LTO4 and LTO7 measured by electrochemical impedance spectroscopy in Ref. 33 is around  $2 \times 10^{-11} \text{ S/m}$ ,  $6 \times 10^{-10} \text{ S/m}$  at  $30^\circ\text{C}$ , which are small compared with the bulk values in the literature:  $10^{-4}$ - $10^{-11} \text{ S/m}$ ,  $1$ - $10^2 \text{ S/m}$ ;<sup>34,36,37</sup> (2) the two electrodes should have different ET resistance due to different deposition temperatures; (3) LTO4 and

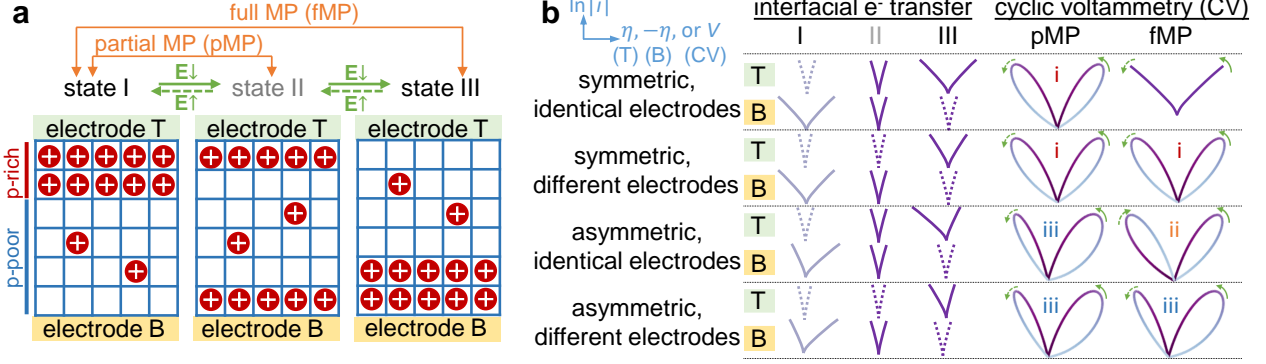


Figure 1: (a) Schematics of the phase re-distribution (state I  $\leftrightarrow$  II  $\leftrightarrow$  III) by applied electric field ( $\mathbf{E}$ , whose direction is  $\uparrow$  or  $\downarrow$ ) between ion-blocking electrodes, which process we refer to as multiphase polarization (MP). (b) The effect of MP on interfacial electron transfer (ET) rates and the resulting total resistance switching characterized by cyclic voltammetry, for different combinations of electrodes. We call an electrode symmetric if it does not conduct current primarily in one direction, and two electrodes identical if they have the same ET rates given the same local concentration and overpotential. The two electrodes can be different due to materials and deposition conditions. Each electrode contact is assumed to be more conductive and symmetric at higher concentration. Each curve represents the log of current ( $\ln|i|$ ) v.s. interfacial overpotential  $\eta$  or  $-\eta$  for the top (T) or bottom (B) electrode at steady state, or v.s. the applied voltage  $V$  for cyclic voltammetry. The ET rates shown by solid curves dominate total resistance. Three patterns of cyclic voltammetry are identified: (i) symmetric pattern with separated states, (ii) symmetric pattern with crossed states, (iii) asymmetric patterns.

LTO7 may not be pure (only Raman spectroscopy was used to estimate Li concentration) and both phases may exist in each memristor; (4) the ET rates usually strongly depend on local ion concentrations.<sup>23,38</sup>

These complex properties, which are not captured by existing theories, motivate us to propose the general MP mechanism, illustrated in Figure 1. We assume that the nanofilm conducts cations and electrons, while the electrodes only conduct electrons. Then cations tend to move along the electric field, but get blocked by the electrodes. Therefore, cations accumulate downstream the electric field, and get depleted on the other side. This phenomenon is called concentration polarization (CP), and is important in many electrochemical systems.<sup>39–50</sup> In multiphase materials, CP should first occur in each phase, and strong enough CP can change phase distribution, which we refer to as multiphase polarization (MP). As shown in Figure 1(a), a downward electric field may drive phase change at the bottom elec-

trode first (I $\rightarrow$ II), and then at the bottom electrode later (II $\rightarrow$ III). We call the process I $\leftrightarrow$ II partial MP (pMP), and I $\leftrightarrow$ III full MP (fMP). The phase distribution should be nonvolatile after removing the applied voltages since phases with different concentration can co-exist in multiphase materials, unlike CP in homogeneous electrolytes. The phase distribution can further influence ET rates on electrodes and thus significantly influence the total resistance if it is dominated by contact resistance, as shown in Figure 1(b). For example, if the two electrodes are symmetric (do not conduct electrons primarily in one direction) but the top electrode is more conductive than the bottom electrode given the same concentration and overpotential, then state I should have larger total resistance than state III, and thus fMP can lead to RS.

To conclude, MP is an interfacial RS mechanism, limited by bulk ion diffusion, which shows multiple, non-volatile resistance states tunable by applied voltages in LTO memristors and other similar systems.

**Model.** Here, we develop an electrochemical phase-field model to quantitatively describe the mechanism, based on nonequilibrium thermodynamics of ion and electron transfer.<sup>23</sup> We neglect temperature variation which should be mild for the interfacial RS mechanism without hot filaments (see the SI), and we neglect mechanical effects for “zero-strain” LTO.<sup>34</sup> Existing phase-field models of ion-intercalation materials in Li-ion batteries<sup>23,51,51–60</sup> and memristors<sup>35</sup> consider only the dynamics of neutral Li<sup>+</sup>-electron pairs. However, here we must account for large electric fields, and broken symmetry between ion and electron transfer at the electrode interfaces. As such, our model includes three charged species: mobile, localized electrons (‘n’), mobile, monovalent cations (‘p’), and fixed, positively charged defects (‘d’). The localized mobile electrons, also called “small polarons” for their coupling with the polarized local environment (including nearby mobile ions), differ from band electrons by a much smaller but thermally-activated mobility and a non-thermally-activated number of mobile electrons. Such electrons are often found in mixed-valency transition metal oxides,<sup>28,61–64</sup> which include some of the most common ion-intercalation materials used in Li-ion batteries

and other applications.<sup>65</sup> The fundamental constants we use include the Boltzmann constant  $k_B$ , temperature  $T$ , electron charge  $e$ , thermal voltage  $V_T = k_B T / e$ , and the Avogadro's number  $N_A$ . We denote the concentration, valence, electrochemical potential, diffusivity, conductivity, flux density of mobile species  $k$  ( $= p, n$ ) as  $c_k$ ,  $z_k$  ( $= \pm 1$ ),  $\mu_k$ ,  $D_k$ ,  $\sigma_k$ ,  $\mathbf{J}_k$ , and the electric potential, current density, time, nanofilm thickness as  $\phi$ ,  $i$ ,  $t$ ,  $h$ . We also define dimensionless variables  $\tilde{c}_k = c_k / c_0$ ,  $\tilde{\mu}_k = \mu_k / k_B T$ ,  $\tilde{\phi} = \phi / V_T$ ,  $\tilde{t} = t / \tau_D = t D_p^0 / h^2$ ,  $\tilde{J}_k = J_k h / D_k^0 c_0$ , and  $\tilde{i} = i / i_D = i / (D_n^0 c_0 N_A e / h)$ , where  $c_0$  and  $D_k^0$  are constants.

First, we enforce electroneutrality:

$$\tilde{c}_p = \tilde{c}_n - \tilde{c}_d = \tilde{c}. \quad (1)$$

Then, we apply a regular solution model with Cahn-Hillard gradient expansion for the two charge carriers ( $k = p, n$ ):<sup>23,63,66–69</sup>

$$\tilde{\mu}_k = \ln \frac{\tilde{c}_k}{\tilde{c}_k^{max} - \tilde{c}_k} + \tilde{\mu}_k^0 + \Omega_k \tilde{c}^\rho + z_k \tilde{\phi} - \kappa_k \tilde{\nabla}^2 \tilde{c}, \quad (2)$$

where the five terms are: ideal entropy for a mixture of charge carriers and vacancies on  $c_k^{max}$  sites, constant standard energy, mixing enthalpy, electrostatic potential energy, and Cahn-Hillard gradient penalty with  $\kappa_n = \kappa_p = \kappa$ . Next, we can use the homogeneous part of  $\tilde{\mu}_p + \tilde{\mu}_n$  (with  $\Omega = \Omega_n + \Omega_p$  defined), to determine the thermal stability (see the SI), including the spinodal points  $\tilde{c}_{s0}$ ,  $\tilde{c}_{s1}$  and the binodal points  $\tilde{c}_{b0}$ ,  $\tilde{c}_{b1}$  (0: ion-poor phase; 1: ion-rich phase). Compared with recent models of Li-ion battery materials,<sup>35,51,59,60,70</sup> this analysis includes the electrochemical potential of electrons, and uses an additional parameter ‘ $\rho$ ’ to adjust concentration-symmetry in the Gibbs free energy of mixing.

Next, we describe the transport of charge carriers by enforcing mass and charge conserva with the generalized Nernst-Planck equation for charge fluxes<sup>23,71</sup>

$$r_k \frac{\partial \tilde{c}_k}{\partial \tilde{t}} + \tilde{\nabla} \cdot \tilde{\mathbf{J}}_k = 0, \quad \tilde{\mathbf{J}}_k = -D_k c_k \nabla \tilde{\mu}_k, \quad (3)$$

where  $\tilde{\nabla} = h\nabla$ ,  $r_p = 1$ ,  $r_n = D_p^0/D_n^0$ . The diffusivity with the excluded volume effects is  $D_k = D_k^0(1 - c_k/c_k^{max})$ , and the corresponding ionic/electronic conductivity is  $\sigma_k = D_k c_k e N_A / V_T$ . We neglect field-dependence of  $D_k^{0,72}$  since we assume most of the electric potential falls at interfaces. The boundary conditions on the electrodes with outward normal vector  $\mathbf{n}$  are: no penetration of ions  $\mathbf{n} \cdot \tilde{\mathbf{J}}_p = 0$ , conservation of electrons  $\mathbf{n} \cdot \tilde{\mathbf{J}}_n = -\mathbf{n} \cdot \tilde{\mathbf{i}}$ , and neutral wetting  $\mathbf{n} \cdot \tilde{\nabla} \tilde{c} = 0$ .

Finally, and critically, we must describe the ion-modulated ET rates at electrode interfaces. At metal-semiconductor interfaces, the ET rates can be described by diffusion, tunneling, or thermo-emission across a Schottky barrier, which can be significantly influenced by doping ions.<sup>38,73,74</sup> However, unlike band conduction in traditional semiconductors, this work focuses on small polaron conduction in mixed-valency intercalation materials. In another words, the bulk ET in LTO and interfacial ET at LTO-Pt interface can be described by  $\text{Ti}^{4+} + \text{Ti}^{3+} \rightleftharpoons \text{Ti}^{3+} + \text{Ti}^{4+}$  and  $\text{Ti}^{4+} + e^-(\text{Pt}) \rightleftharpoons \text{Ti}^{3+}$ , respectively. This ET mechanism, though in solids, is very analogous to the ET reactions in liquid solutions and at liquid-solid interfaces as described by Marcus theory,<sup>64,75</sup> which involves a microscopic picture of solvent fluctuation and predicts curved Tafel plots (log current v.s. voltage) at large overpotentials as observed in experiments.<sup>76-81</sup> Recently, Marcus theory was also applied to solid-state ET in carbon-coated lithium iron phosphate.<sup>75</sup> However, the original Marcus theory and the asymmetric Marcus theory which has very limited applicability<sup>82-84</sup> cannot capture the significant asymmetry possibly seen at solid-solid interfaces. Then we notice the facts that Marcus theory reduces to the phenomenological Butler-Volmer (BV) equation at small to medium overpotentials,<sup>23,81,85,86</sup> and BV equation with a series resistance can also lead to curved Tafel plots.<sup>51</sup> Though usually used for ion transfer, BV equation can be used for general Faraday reactions<sup>23</sup> including  $\text{Ti}^{4+} + e^-(\text{Pt}) \rightleftharpoons \text{Ti}^{3+}$ . Actually a Schottky diode is also usually described by a BV-form formula in combination with a series resistance to fit the curved Tafel plots,<sup>38,87,88</sup> though the ion-modulated exchange current should be different from the system we study here. As a first approximation to capture these diverse

phenomena, we propose the following generalized BV equation, which includes non-ideal thermodynamics to capture the concentration dependence and a series resistance  $\tilde{R}_s$  to serve a similar role as Marcus theory to curve the Tafel plots:<sup>23,51</sup>

$$\mathbf{n} \cdot \tilde{\mathbf{i}} = \text{Da} f(\tilde{c}; \alpha) g(\tilde{\eta}; \alpha) e^{-\alpha \kappa \tilde{V}^2 \tilde{c}}, \quad (4a)$$

$$f(\tilde{c}; \alpha) = (\tilde{c}_n / \tilde{c}_n^{max})^\alpha (1 - \tilde{c}_n / \tilde{c}_n^{max})^{1-\alpha} e^{\alpha \Omega_n \tilde{c}^\rho}, \quad (4b)$$

$$g(\tilde{\eta}; \alpha) = e^{(1-\alpha)\tilde{\eta}} - e^{-\alpha\tilde{\eta}}, \quad (4c)$$

where  $\tilde{\eta} = \tilde{\mu}_n - \tilde{\mu}_e$  is the overpotential across the interface,  $\tilde{\mu}_e = \tilde{\mu}_e^0 - \tilde{\phi}_e$  is the Fermi energy in the electrode, and  $\tilde{\phi}_e^B = 0$ ,  $\tilde{\phi}_e^T = \tilde{V} - \tilde{I}\tilde{R}_s$  (where  $\tilde{I}$  is the total current and in 1D  $\tilde{I} = \tilde{i} = \tilde{\mathbf{i}} \cdot \mathbf{e}_x$ ,  $\tilde{V}$  is the applied voltage, ‘T’ and ‘B’ represent the two electrodes at top and bottom). We further assume  $\alpha = \alpha_0 + (0.5 - \alpha_0)\tilde{c}$  so that ET asymmetry disappears for large  $\tilde{c}$  (Ohmic contact). Constants Da and  $\alpha^0$  can be different for the two electrodes. See the SI for derivation of Equation 4.

**Dimensionless Results.** We proceed to use our model to analyze RS performance of multiphase ion-intercalation nanofilms<sup>4</sup> in terms of dimensionless variables. As an example to test the model, we choose parameters based on the LTO material<sup>24,34,36,37,71,89,90</sup> (see the SI):  $\tilde{c}_p^{max} = 1$ ,  $\tilde{c}_n^{max} = 5/3$ ,  $\Omega = -12$ ,  $\rho = 0.7$ ,  $\kappa = 1.1 \times 10^{-3}$ ,  $\Omega_n = 20$ ,  $D_p/D_n = 10^{-5}$ , and  $\tilde{c}_d = 0.01$ , and  $\tilde{R}_s = 100$ . Note that these values are all obtained/estimated from the experiments in the literature without fitting, and especially,  $\tilde{R}_s$  is estimated from the reorganization energy of the small polarons.

We first analyze switching current and time, based on 1D simulations of MP in response to a step current (no need to consider ET here) as shown in Figure 2. Figure 2(a) shows two typical cases. Both cases reach steady state during the applied current, but only the larger current causes MP, in which case the time scale ( $\tilde{\tau}^T, \tilde{\tau}^B$ ) for phase change at the two electrodes can be determined. The smaller one of  $\tilde{\tau}^T, \tilde{\tau}^B$  is the time for pMP to occur, while the larger one is for fMP to occur. Then the switching current and time for more cases with

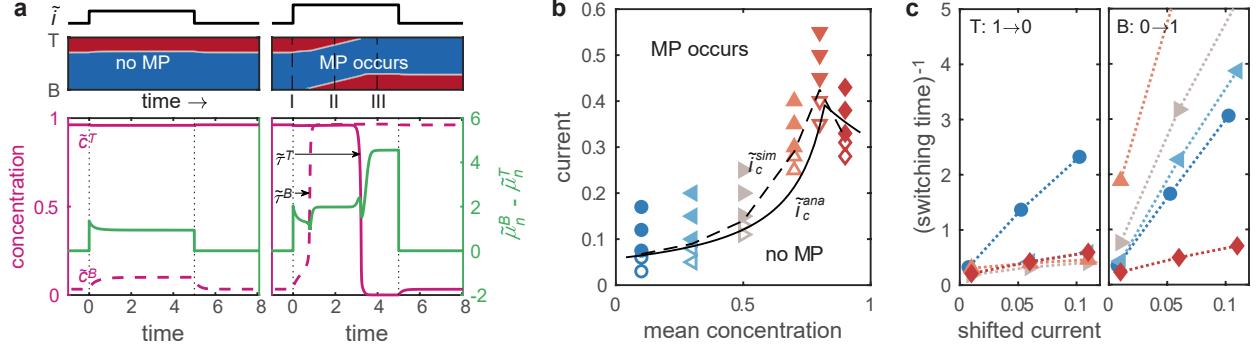


Figure 2: The switching current and switching time from simulations of step current response. (a) From top to bottom: applied current ( $\tilde{i} = i/i_D$ ), phase distribution (contour map, red: ion-rich phase 1, blue: ion-poor phase 0), boundary concentrations ( $\tilde{c}^T$ ,  $\tilde{c}^B$ ), electrochemical potential drop ( $\tilde{\mu}_n^B - \tilde{\mu}_n^T$ ), along with time ( $\tilde{t} = t/\tau_D$ ) for two typical cases (with mean concentration  $\tilde{c}_m = 0.3$ , current plateau  $\tilde{i}_{max} = 0.08, 0.12$ ). The schematics for the three typical states I, II, III during MP can be found in Figure 1. The switching time  $\tilde{\tau}$  can be obtained from  $\tilde{\tau}^T = \tilde{t}|_{\tilde{c}^T=0.5}$  and  $\tilde{\tau}^B = \tilde{t}|_{\tilde{c}^B=0.5}$ . (b) The critical current ( $\tilde{i}_c$ ) for MP to occur indicated by simulations (filled and empty markers to indicate MP and no MP, dashed line for eye guidance) and theory (solid line), for different mean concentration ( $\tilde{c}_m$ ). (c) The inverse of the switching time  $1/\tilde{\tau}$  along with the shifted current ( $\tilde{i} - \tilde{i}_c^{ana}$ ). The colors and markers to label concentrations in (b)(c) are consistent.

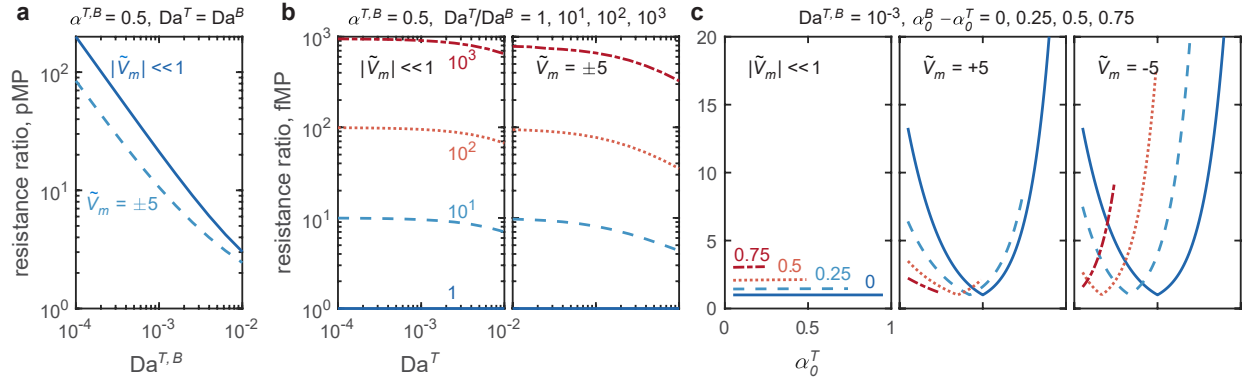


Figure 3: The resistance ratio ( $\mathcal{R}$ ) measured at different voltages ( $\tilde{V}_m = V_m/V_T$ ) due to (a) pMP and identical, symmetric electrodes, and (b) fMP and symmetric electrodes with various rate constants  $Da$ , (c) fMP and asymmetric electrodes with the same  $Da$ . For pMP,  $\mathcal{R} = \exp(|\ln \frac{\tilde{R}(\tilde{c}_{b1}, \tilde{c}_{b0})}{\tilde{R}(\tilde{c}_{b1}, \tilde{c}_{b1})}|)$ . For fMP,  $\mathcal{R} = \exp(|\ln \frac{\tilde{R}(\tilde{c}_{b1}, \tilde{c}_{b0})}{\tilde{R}(\tilde{c}_{b0}, \tilde{c}_{b1})}|)$ . Here we choose  $\tilde{c}_m = 0.5$  to calculate the bulk resistance.

different averaged concentration  $\tilde{c}_m$  and applied current  $\tilde{i}$  are summarized in Figure 2(b)(c). The condition under which MP occurs can be explained as follows. In each phase, the concentration rises at the downstream of the electric field and falls on the other side. If this

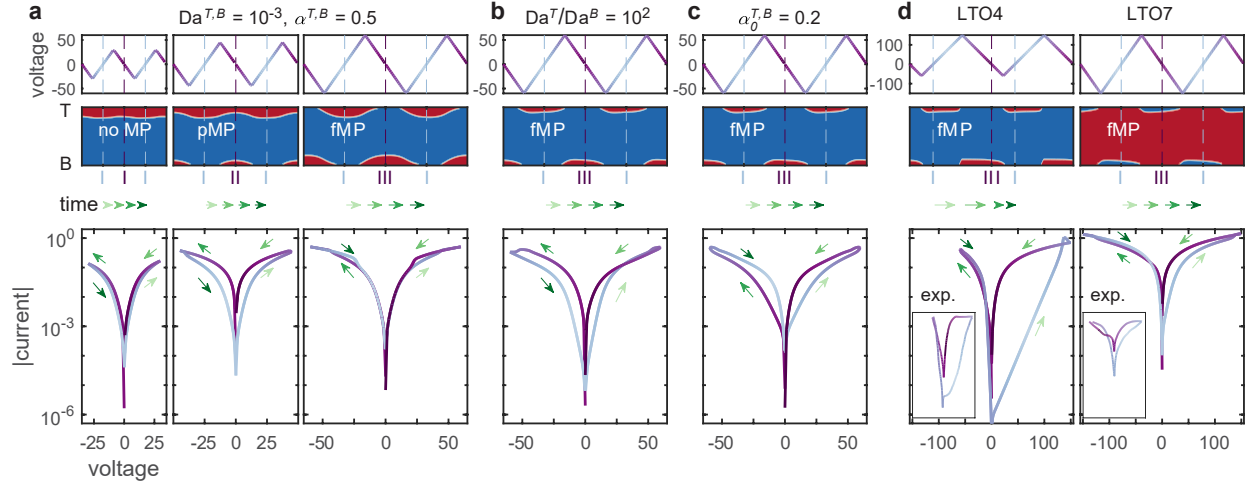


Figure 4: Simulation results of cyclic voltammetry for two cycles. From top to bottom: applied voltage ( $\tilde{V} = V/V_T$ ) versus time ( $\tilde{t} = t/\tau_D$ ), phase distribution (red: ion-rich phase 1, blue: ion-poor phase 0) versus time ( $\tilde{t}$ ), and current  $|\tilde{i}| = |i/i_D|$  versus voltage ( $\tilde{V}$ ). The sweeping rate is 125 in dimensionless scale, or 50 mV/s if the diffusion time  $\tau_D = 64$  s. Four sets of electrodes are considered: (a) identical, symmetric electrodes with three maximum sweeping voltages, (b) symmetric, different electrodes, (c) identical, asymmetric electrodes, (d) different, asymmetric electrodes to fit for experiments of LTO4 and LTO7 memristors from Ref. 33. The dashed lines in the time evolution figures label three typical states, and schematics for state I, II, III can be found in Figure 1. Interfacial parameters not shown in the figure: (b)  $\text{Da}^T = 10^{-2}$ , (c)  $\text{Da}^{T,B} = 10^{-3}$ , (d) LTO4:  $\text{Da}^T = 10^{-3}$ ,  $\text{Da}^B = 10^{-6}$ ,  $\alpha_0^T = 0.3$ ,  $\alpha_0^B = 0.08$ , LTO7:  $\text{Da}^T = 10^{-1}$ ,  $\text{Da}^B = 10^{-3}$ ,  $\alpha_0^T = 0.05$ ,  $\alpha_0^B = 0.2$ . Mean concentration:  $\tilde{c}_m = 0.2, 0.1, 0.1, 0.1, 0.9$  for (a), (b), (c), (d)LTO4, (d)LTO7.

perturbation in either phase is large enough to cause phase change, MP occurs. We also derive an approximate, analytical expression for the critical current:

$$\tilde{i}_c^{ana} = \min \left\{ \frac{\mathcal{F}|_{\tilde{c}_{b0}}^{\tilde{c}_{s0}}}{\tilde{h}_0(\tilde{c}_m)}, \frac{\mathcal{F}|_{\tilde{c}_{s1}}^{\tilde{c}_{b1}}}{1 - \tilde{h}_0(\tilde{c}_m)} \right\}, \quad (5)$$

where  $\mathcal{F}(\tilde{c})$  is the effective potential for current ( $\tilde{i} = \tilde{\nabla}_x \mathcal{F}$ ),  $\tilde{h}_0(\tilde{c})$  is an estimate of the occupation of the ion-poor phase 0 (see the SI). This expression is consistent with simulations, as shown in Figure 2(b). For the switching time, we find that its reciprocal is roughly proportional to the current, as shown in Figure 2(c). We also find that the end concentrations ( $\tilde{c} = 0.1, 0.9$ ) have similar switching time on the two sides, in which cases pMP is unlikely to be observed. And the  $\tilde{c} = 0.1$  case switches faster than  $\tilde{c} = 0.9$ . At medium concentrations, there is a big time window between pMP and fMP, which makes it possible to utilize pMP for RS.

Next, we analyze the resistance ratio (measured by voltage  $\tilde{V}_m$ ) for different combinations of interfacial ET parameters. Here we consider steady state and assume  $|\tilde{V}_m|$  is not large enough to significantly perturb the bulk concentration profiles. If  $|\tilde{V}_m| \ll 1$ , the total resistance is  $\tilde{R}(\tilde{c}^T, \tilde{c}^B) = \frac{1}{\text{Da}^T f(\tilde{c}^T; \alpha^T)} + \frac{1}{\text{Da}^B f(\tilde{c}^B; \alpha^B)} + \tilde{R}_b + \tilde{R}_s$ , where  $\tilde{R}_b$  is the bulk resistance and is usually much smaller than the other resistances (see the SI). If  $|\tilde{V}_m| > 1$ , we need to solve  $\tilde{R}$  from the current balance. Then we can compare  $\tilde{R}$  for different states and calculate the resistance ratio  $\mathcal{R}$  ( $\geq 1$  by definition), as shown in Figure 3. First, we need to know when MP can lead to RS ( $\mathcal{R} > 1$ ). Basically, for symmetric, identical electrodes, only pMP can lead to RS (see Figure 3(a) and  $\text{Da}^T/\text{Da}^B = 1$  case in Figure 3(b)). For other cases, fMP can also lead to RS. Then, to get a larger  $\mathcal{R}$ , the ET on the two electrodes should dominate the total resistance and be very different after MP. Therefore, larger  $\Omega_n$  (more Fermi energy lift due to ion intercalation) is preferred. In addition, for symmetric electrodes,  $\mathcal{R}$  should decrease for larger Da, smaller Da ratios, larger  $|\tilde{V}_m|$ , as shown in Figure 3(a)(b). For asymmetric electrodes, the situation is more complex. Both the magnitude and sign of  $\tilde{V}_m$

are very important, as shown in Figure 3(c). Only large enough  $|\tilde{V}_m|$  can lead to  $\mathcal{R} > 1$  for identical, asymmetric electrodes and fMP (solid lines). Moreover,  $\mathcal{R}$  for asymmetric, different electrodes depends on the sign of  $\tilde{V}_m$ .

Finally, we analyze the cyclic voltammetry behaviors. As expected (Figure 1), for symmetric and identical electrodes, only pMP can lead to RS, as shown in Figure 4(a). A Da ratio and fMP can lead to separated states (Figure 4(b)), while asymmetric  $\alpha$  and fMP can lead to crossed states (Figure 4(c)), around zero voltage.

**Comparison with experiments.** For dimensional analysis, we use additional parameters:  $c_0 = 22 \text{ M}$ ,  $h = 80 \text{ nm}$ , electrode area  $S = 500 \mu\text{m} \times 500 \mu\text{m}$ ,  $D_p^0 = 1 \times 10^{-16} \text{ m}^2/\text{s}$  (see the SI). The theory works well for the LTO memristors<sup>33</sup> in terms of the following three aspects.

First, the theory predicts that the switching time is limited by the ion diffusion time ( $\tau_D = 64 \text{ s}$ ), though it can be reduced by over ten times by increasing the current (Figure 2). Therefore, we predict switching time in seconds, which is consistent with experiments.

Second, without any fitting parameters, our theory indicates that LTO4 memristor should have faster switching than LTO7 and need less current (case  $c = 0.1, 0.9$  in Figure 2), which are also consistent with Figure 2(c)(d) in Ref. 33.

Finally, by choosing proper interfacial parameters, we can obtain cyclic voltammetry patterns similar to experiments (Figure 2(a)(b) in Ref. 33), as shown in Figure 4(d). Note that the dimensionless current at low and high voltage is mainly determined by Da and  $\tilde{R}_s$ , respectively; and the dimensional current scale is mainly determined by the diffusion current  $i_D$ . Since electronic conductivity can vary by magnitudes due to defects,<sup>36,37</sup> we may assume LTO7 conductivity to be  $\sim 0.005 \text{ S/m}$  to quantitatively fit the experimental current in Figure 4(d) (see the SI).

However, the 1D simple picture cannot predict the numerous resistance states and finite retention time observed in experiments. These issues may be explained by 2D or 3D phase nucleation, which may also reduce the switching current significantly..

**Discussion and perspectives.** Our model provides some fresh insights into the optimization and possible alternative designs for MP-based memristors.

First, the switching time of existing LTO memristors (on the order of seconds) is too long for the requirements of in-memory computing, including neuromorphic artificial synapses ( $\leq \mu\text{s-ms}$ )<sup>91</sup> and digital computing ( $\leq \text{ns}$ ).<sup>3</sup> The performance can be improved by changing from LTO to intercalation materials with high ion mobility, decreasing nanofilm thickness, or increasing current. For example, we can choose intercalation materials with lower-dimensional diffusion paths (Figure 5(a)), e.g., nano-sized LFP (defects-sensitive 1D paths),<sup>92</sup> layered materials (2D paths)<sup>21</sup> like  $\text{MoS}_2$ ,<sup>93-95</sup> LCO,<sup>96</sup> graphite,<sup>19,97</sup> and even 2D materials (with only a few layers).<sup>20,98</sup> The ion diffusivity for these examples are shown in Figure 5(b). Note that these intercalation materials all have phase separation and strong concentration dependence of conductance (thus usually of contact resistance), which is necessary for MP-induced RS. We then assume the nanofilm thickness is 50 nm and the switching time is one-tenth of the diffusion time, and put the axes for diffusion and switching time in Figure 5(b). This is a conservative estimation, but note that we need a thick enough nanofilm to allow co-existence of different phases, and a too large current may lead to problems like Li plating. As we can see, we should be able to obtain switching time of  $\mu\text{s-ms}$  which is sufficient for neuromorphic computing.

In addition, the theory implicitly indicates infinite retention time, without state decay by diffusion which usually occurs for traditional interfacial mechanisms.<sup>15</sup> The experimental finite retention time may come from rich-phase detachment from electrodes due to material heterogeneity, surface wetting, or thermal fluctuation. This can be (partially) avoided by surface processing and scale-down, which should also help increase recyclability and reduce stochasticity. Finally, scale-down should be the primary way to reduce power consumption.

More discussion can be found in the SI.

**Conclusion.** In this work, we have proposed and modeled a new interfacial resistive-switching mechanism, multiphase polarization, for a system composed of a multiphase, ion-

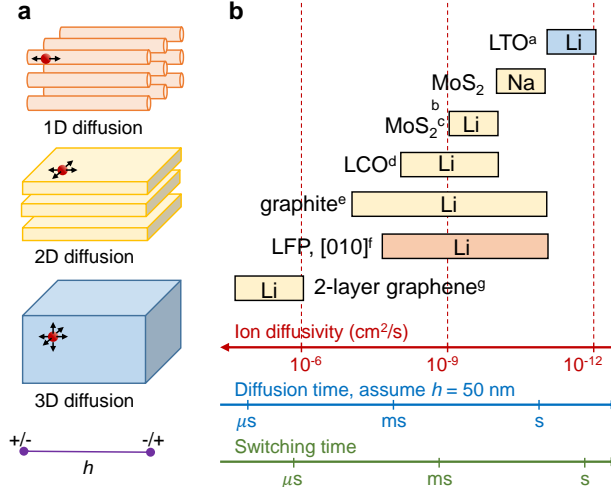


Figure 5: The scales of ion diffusivity (at room temperature), diffusion time, and switching time by multiphase polarization, for several ion-intercalation materials. We assume the length scale between electrodes ( $h$ ) to be 50 nm to calculate the diffusion time, and we estimate the switching time to be one-tenth of the diffusion time at certain current. The colors labeling diffusion path dimensions in (a) are consistent with the colors for different materials in (b). References: <sup>a</sup>Ref. 19, <sup>b</sup>Ref. 93, <sup>c</sup>Refs. 94,95, <sup>d</sup>Ref. 96, <sup>e</sup>Ref. 19, <sup>f</sup>Ref. 92, <sup>g</sup>Ref. 98.

intercalation nanofilm sandwiched by two ion-blocking electrodes. This model is the first to qualitatively explain the complex RS dynamics of LTO memristors, and it provides insights for device optimization and new designs. Future theoretical work could account for 2D or 3D phase nucleation at interfaces,<sup>56,99</sup> thermal and mechanical effects,<sup>55,57</sup> and multi-stage phase separation.<sup>58</sup>

## Acknowledgement

This work was supported by a grant from Ericsson. The authors would like to thank Danniell Cogswell, Willis O’Leary, Dimitrios Fraggadakis, Moran Balaish, Drew Buzzell, Jennifer Rupp, Ju Li, and Pedro de Souza for helpful discussions.

## Supporting Information Available

The Supporting information is available free of charge at <https://pubs.acs.org/doi/10.1021/acs.nanolett.2c01765>.

Details on the dielectric breakdown model; temperature effect; thermal stability analysis; derivation of the generalized Butler-Volmer equation, threshold current, and resistance ratio; parameters; numerical method; additional discussion.

## References

- (1) Waser, R.; Dittmann, R.; Staikov, C.; Szot, K. Redox-based resistive switching memories nanoionic mechanisms, prospects, and challenges. Advanced Materials **2009**, 21, 2632–2663.
- (2) Jeong, D. S.; Thomas, R.; Katiyar, R. S.; Scott, J. F.; Kohlstedt, H.; Petraru, A.; Hwang, C. S. Emerging memories: Resistive switching mechanisms and current status. Reports on Progress in Physics **2012**, 75, 076502.
- (3) Ielmini, D.; Wong, H. S. In-memory computing with resistive switching devices. Nature Electronics **2018**, 1, 333–343.
- (4) Waser, R.; Dittmann, R.; Menzel, S.; Noll, T. Introduction to new memory paradigms: Memristive phenomena and neuromorphic applications. Faraday Discussions **2019**, 213, 11–27.
- (5) Li, Y.; Ang, K.-W. Hardware Implementation of Neuromorphic Computing Using Large-Scale Memristor Crossbar Arrays. Advanced Intelligent Systems **2021**, 3, 2000137.
- (6) Zidan, M. A.; Strachan, J. P.; Lu, W. D. The future of electronics based on memristive systems. Nature Electronics **2018**, 1, 22–29.

- (7) Sawa, A. Resistive switching in transition metal oxides. Materials Today **2008**, 11, 28–36.
- (8) Valov, I.; Waser, R.; Jameson, J. R.; Kozicki, M. N. Electrochemical metallization memories - Fundamentals, applications, prospects. Nanotechnology **2011**, 22, 254003.
- (9) Ielmini, D. Resistive switching memories based on metal oxides: Mechanisms, reliability and scaling. Semiconductor Science and Technology **2016**, 31, 063002.
- (10) Wang, Z.; Wu, H.; Burr, G. W.; Hwang, C. S.; Wang, K. L.; Xia, Q.; Yang, J. J. Resistive switching materials for information processing. Nature Reviews Materials **2020**, 5, 173–195.
- (11) Del Valle, J.; Ramírez, J. G.; Rozenberg, M. J.; Schuller, I. K. Challenges in materials and devices for resistive-switching-based neuromorphic computing. Journal of Applied Physics **2018**, 124, 211101.
- (12) Ding, K.; Wang, J.; Zhou, Y.; Tian, H.; Lu, L. L.; Mazzarello, R.; Jia, C.; Zhang, W.; Rao, F.; Ma, E. Phase-change heterostructure enables ultralow noise and drift for memory operation. Science **2019**, 366, 210–215.
- (13) Wong, H. S.; Raoux, S.; Kim, S.; Liang, J.; Reifenberg, J. P.; Rajendran, B.; Asheghi, M.; Goodson, K. E. Phase change memory. Proceedings of the IEEE **2010**, 98, 2201–2227.
- (14) Zhang, K.; Wang, J.; Huang, Y.; Chen, L. Q.; Ganesh, P.; Cao, Y. High-throughput phase-field simulations and machine learning of resistive switching in resistive random-access memory. npj Computational Materials **2020**, 6, 1–10.
- (15) Sassine, G.; La Barbera, S.; Najjari, N.; Minvielle, M.; Dubourdieu, C.; Alibart, F. Interfacial versus filamentary resistive switching in TiO<sub>2</sub> and HfO<sub>2</sub> devices . Journal

- of Vacuum Science & Technology B, Nanotechnology and Microelectronics: Materials, Processing, Measurement, and Phenomena **2016**, 34, 012202.
- (16) Hur, J. H.; Lee, M. J.; Lee, C. B.; Kim, Y. B.; Kim, C. J. Modeling for bipolar resistive memory switching in transition-metal oxides. Physical Review B - Condensed Matter and Materials Physics **2010**, 82, 1–5.
  - (17) Yang, J. J.; Pickett, M. D.; Li, X.; Ohlberg, D. A.; Stewart, D. R.; Williams, R. S. Memristive switching mechanism for metal/oxide/metal nanodevices. Nature Nanotechnology **2008**, 3, 429–433.
  - (18) Solanki, A.; Guerrero, A.; Zhang, Q.; Bisquert, J.; Sum, T. C. Interfacial Mechanism for Efficient Resistive Switching in Ruddlesden-Popper Perovskites for Non-volatile Memories. Journal of Physical Chemistry Letters **2020**, 11, 463–470.
  - (19) Nitta, N.; Wu, F.; Lee, J. T.; Yushin, G. Li-ion battery materials: Present and future. Materials Today **2015**, 18, 252–264.
  - (20) Stark, M. S.; Kuntz, K. L.; Martens, S. J.; Warren, S. C. Intercalation of Layered Materials from Bulk to 2D. Advanced Materials **2019**, 31, 1808213.
  - (21) Zhou, J.; Lin, Z.; Ren, H.; Duan, X.; Shakir, I.; Huang, Y.; Duan, X. Layered Intercalation Materials. Advanced Materials **2021**, 33, 2004557.
  - (22) Riess, I. Electrochemistry of mixed ionic-electronic conductors. CRC Handbook of Solid State Electrochemistry **1997**, 223–268.
  - (23) Bazant, M. Z. Theory of chemical kinetics and charge transfer based on nonequilibrium thermodynamics. Accounts of Chemical Research **2013**, 46, 1144–1160.
  - (24) Morgan, B. J.; Carrasco, J.; Teobaldi, G. Variation in surface energy and reduction drive of a metal oxide lithium-ion anode with stoichiometry: A DFT study of lithium titanate spinel surfaces. Journal of Materials Chemistry A **2016**, 4, 17180–17192.

- (25) Liu, Y.; Lian, J.; Sun, Z.; Zhao, M.; Shi, Y.; Song, H. The first-principles study for the novel optical properties of  $\text{LiTi}_2\text{O}_4$ ,  $\text{Li}_4\text{Ti}_5\text{O}_{12}$ ,  $\text{Li}_2\text{Ti}_2\text{O}_4$  and  $\text{Li}_7\text{Ti}_5\text{O}_{12}$ . Chemical Physics Letters **2017**, 677, 114–119.
- (26) Yao, X.; Klyukin, K.; Lu, W.; Onen, M.; Ryu, S.; Kim, D.; Emond, N.; Waluyo, I.; Hunt, A.; del Alamo, J. A.; Li, J.; Yildiz, B. Protonic solid-state electrochemical synapse for physical neural networks. Nature Communications **2020**, 11, 1–10.
- (27) Gellings, P. J.; Bouwmeester, H. CRC Press; 1997.
- (28) Cox, P. A. Transition metal oxides: an introduction to their electronic structure and properties; Oxford University Press, 2010; Vol. 27.
- (29) Nguyen, V. S. et al. Direct Evidence of Lithium Ion Migration in Resistive Switching of Lithium Cobalt Oxide Nanobatteries. Small **2018**, 14, 1–7.
- (30) Sharbati, M. T.; Du, Y.; Torres, J.; Ardolino, N. D.; Yun, M.; Xiong, F. Low-Power, Electrochemically Tunable Graphene Synapses for Neuromorphic Computing. Advanced Materials **2018**, 30, 1802353.
- (31) Fuller, E. J.; Gabaly, F. E.; Léonard, F.; Agarwal, S.; Plimpton, S. J.; Jacobs-Gedrim, R. B.; James, C. D.; Marinella, M. J.; Talin, A. A. Li-Ion Synaptic Transistor for Low Power Analog Computing. Advanced Materials **2017**, 29, 1–8.
- (32) Onen, M.; Emond, N.; Li, J.; Yildiz, B.; Del Alamo, J. A. CMOS-Compatible Protonic Programmable Resistor Based on Phosphosilicate Glass Electrolyte for Analog Deep Learning. Nano Letters **2021**, 21, 6111–6116.
- (33) Gonzalez-Rosillo, J. C.; Balaish, M.; Hood, Z. D.; Nadkarni, N.; Fraggadakis, D.; Kim, K. J.; Mullin, K. M.; Pfenninger, R.; Bazant, M. Z.; Rupp, J. L. Lithium-Battery Anode Gains Additional Functionality for Neuromorphic Computing through Metal–Insulator Phase Separation. Advanced Materials **2020**, 32, 1–12.

- (34) Zhao, B.; Ran, R.; Liu, M.; Shao, Z. A comprehensive review of  $\text{Li}_4\text{Ti}_5\text{O}_{12}$ -based electrodes for lithium-ion batteries : The latest advancements and future perspectives. Materials Science and Engineering R **2015**, 98, 1–71.
- (35) Fraggedakis, D.; Mirzadeh, M.; Zhou, T.; Bazant, M. Z. Dielectric Breakdown by Electric-field Induced Phase Separation. Journal of The Electrochemical Society **2020**, 167, 113504.
- (36) Young, D.; Ransil, A.; Amin, R.; Li, Z.; Chiang, Y. M. Electronic conductivity in the  $\text{Li}_4/3\text{Ti}_5/3\text{O}_4\text{-Li}_7/3\text{Ti}_5/3\text{O}_4$  system and variation with state-of-charge as a Li battery anode. Advanced Energy Materials **2013**, 3, 1125–1129.
- (37) Scharner, S.; Weppner, W.; Schmid-Beurmann, P. Evidence of Two-Phase Formation upon Lithium Insertion into the  $\text{Li}_{1.33}\text{Ti}_{1.67}\text{O}_4$  Spinel. Journal of The Electrochemical Society **1999**, 146, 857–861.
- (38) Sze, S. M.; Ng, K. K. Physics of Semiconductor Devices; John Wiley & Sons, 2007.
- (39) Mani, A.; Zangle, T. A.; Santiago, J. G. On the Propagation of Concentration Polarization from Microchannel-Nanochannel Interfaces Part I: Analytical Model and Characteristic Analysis. Langmuir **2009**, 25, 3898–3908.
- (40) Zangle, T. A.; Mani, A.; Santiago, J. G. On the Propagation of Concentration Polarization from Microchannel-Nanochannel interfaces Part II: Numerical and experimental study. Langmuir **2009**, 25, 3909–3916.
- (41) Dydek, E. V.; Zaltzman, B.; Rubinstein, I.; Deng, D. S.; Mani, A.; Bazant, M. Z. Overlimiting current in a microchannel. Physical Review Letters **2011**, 107, 1–5.
- (42) Dydek, E. V.; Bazant, M. Z. Nonlinear dynamics of ion concentration polarization in porous media: The leaky membrane model. AIChE Journal **2013**, 59, 3539–3555.

- (43) Nielsen, C. P.; Bruus, H. Concentration polarization, surface currents, and bulk advection in a microchannel. Physical Review E - Statistical, Nonlinear, and Soft Matter Physics **2014**, 90, 1–14.
- (44) Mishchuk, N. A. Concentration polarization of interface and non-linear electrokinetic phenomena. Advances in Colloid and Interface Science **2010**, 160, 16–39.
- (45) Andersen, M. B.; Van Soestbergen, M.; Mani, A.; Bruus, H.; Biesheuvel, P. M.; Bazant, M. Z. Current-induced membrane discharge. Physical Review Letters **2012**, 109, 1–5.
- (46) Schlumpberger, S.; Lu, N. B.; Suss, M. E.; Bazant, M. Z. Scalable and Continuous Water Deionization by Shock Electrodialysis. Environmental Science and Technology Letters **2015**, 2, 367–372.
- (47) Mani, A.; Bazant, M. Z. Deionization shocks in microstructures. Physical Review E - Statistical, Nonlinear, and Soft Matter Physics **2011**, 84, 1–13.
- (48) Tian, H.; Alkhadra, M. A.; Bazant, M. Z. Theory of shock electrodialysis I: Water dissociation and electrosmotic vortices. Journal of Colloid and Interface Science **2021**, 589, 605–615.
- (49) Tian, H.; Alkhadra, M. A.; Bazant, M. Z. Theory of shock electrodialysis II: Mechanisms of selective ion removal. Journal of Colloid and Interface Science **2021**, 589, 616–621.
- (50) Tian, H.; Alkhadra, M. A.; Conforti, K. M.; Bazant, M. Z. Continuous and Selective Removal of Lead from Drinking Water by Shock Electrodialysis. ACS ES&T Water **2021**, 1, 2269–2274.
- (51) Smith, R. B.; Bazant, M. Z. Multiphase Porous Electrode Theory. Journal of The Electrochemical Society **2017**, 164, E3291–E3310.

- (52) Singh, G. K.; Ceder, G.; Bazant, M. Z. Intercalation dynamics in rechargeable battery materials: General theory and phase-transformation waves in  $\text{LiFePO}_4$ . Electrochimica Acta **2008**, 53, 7599–7613.
- (53) Tang, M.; Huang, H.-Y.; Meethong, N.; Kao, Y.-H.; Carter, W. C.; Chiang, Y.-M. Model for the particle size, overpotential, and strain dependence of phase transition pathways in storage electrodes: application to nanoscale olivines. Chemistry of Materials **2009**, 21, 1557–1571.
- (54) Bai, P.; Cogswell, D. A.; Bazant, M. Z. Suppression of phase separation in  $\text{LiFePO}_4$  nanoparticles during battery discharge. Nano Letters **2011**, 11, 4890–4896.
- (55) Cogswell, D. A.; Bazant, M. Z. Coherency Strain and the Kinetics of Phase Separation in  $\text{Li}_x\text{FePO}_4$  Nanoparticles. Acs Nano **2012**, 6, 2215–2225.
- (56) Cogswell, D. A.; Bazant, M. Z. Theory of coherent nucleation in phase-separating nanoparticles. Nano Letters **2013**, 13, 3036–3041.
- (57) Nadkarni, N.; Rejovitsky, E.; Fraggedakis, D.; Di Leo, C. V.; Smith, R. B.; Bai, P.; Bazant, M. Z. Interplay of phase boundary anisotropy and electro-auto-catalytic surface reactions on the lithium intercalation dynamics in  $\text{LiXFePO}_4$  plateletlike nanoparticles. Physical Review Materials **2018**, 2, 1–13.
- (58) Smith, R. B.; Khoo, E.; Bazant, M. Z. Intercalation kinetics in multiphase-layered materials. The Journal of Physical Chemistry C **2017**, 121, 12505–12523.
- (59) Nadkarni, N.; Zhou, T.; Fraggedakis, D.; Gao, T.; Bazant, M. Z. Modeling the Metal–Insulator Phase Transition in  $\text{Li}_x\text{CoO}_2$  for Energy and Information Storage. Advanced Functional Materials **2019**, 29, 1–9.
- (60) De Klerk, N. J.; Vasileiadis, A.; Smith, R. B.; Bazant, M. Z.; Wagemaker, M. Explaining

- key properties of lithiation in TiO<sub>2</sub> -anatase Li-ion battery electrodes using phase-field modeling. Physical Review Materials **2017**, 1, 1–13.
- (61) Bosman, A. J.; van Daal, H. J. Small-polaron versus band conduction in some transition-metal oxides. Advances in Physics **1970**, 19, 1–117.
- (62) Ellis, B.; Perry, L. K.; Ryan, D. H.; Nazar, L. F. Small polaron hopping in Li<sub>x</sub>FePO<sub>4</sub> solid solutions: Coupled lithium-ion and electron mobility. Journal of the American Chemical Society **2006**, 128, 11416–11422.
- (63) Zhou, F.; Maxisch, T.; Ceder, G. Configurational electronic entropy and the phase diagram of mixed-valence oxides: The case of Li<sub>x</sub>FePO<sub>4</sub>. Physical Review Letters **2006**, 97, 155704.
- (64) Mikkelsen, K. V.; Ratner, M. A. Electron Tunneling in Solid-State Electron-Transfer Reactions. Chemical Reviews **1987**, 87, 113–153.
- (65) Sood, A.; Poletayev, A. D.; Cogswell, D. A.; Csernica, P. M.; Mefford, J. T.; Fraggedakis, D.; Toney, M. F.; Lindenberg, A. M.; Bazant, M. Z.; Chueh, W. C. Electrochemical ion insertion from the atomic to the device scale. Nature Reviews Materials **2021**, 6, 847–867.
- (66) Mebane, D. S.; De Souza, R. A. A generalised space-charge theory for extended defects in oxygen-ion conducting electrolytes: from dilute to concentrated solid solutions. Energy and Environmental Science **2015**, 8, 2935–2940.
- (67) Guyer, J. E.; Boettinger, W. J.; Warren, J. A.; McFadden, G. B. Phase field modeling of electrochemistry. I. Equilibrium. Physical Review E - Statistical, Nonlinear, and Soft Matter Physics **2004**, 69, 1–13.
- (68) Guyer, J. E.; Boettinger, W. J.; Warren, J. A.; McFadden, G. B. Phase field modeling of

- electrochemistry. II. Kinetics. Physical Review E - Statistical Physics, Plasmas, Fluids, and Related Interdisciplinary Topics **2004**, 69, 12.
- (69) Cahn, J. W.; Hilliard, J. E. Free energy of a nonuniform system. I. Interfacial free energy. The Journal of Chemical Physics **1958**, 28, 258–267.
- (70) Zhao, H.; Storey, B. D.; Braatz, R. D.; Bazant, M. Z. Learning the Physics of Pattern Formation from Images. Physical Review Letters **2020**, 124, 60201.
- (71) Maier, J. Physical Chemistry of Ionic Materials: Ions and Electrons in Solids; John Wiley & Sons, Ltd, 2004.
- (72) Menzel, S.; Von Witzleben, M.; Havel, V.; Böttger, U. The ultimate switching speed limit of redox-based resistive switching devices. Faraday Discussions **2019**, 213, 197–213.
- (73) Tung, R. T. The physics and chemistry of the Schottky barrier height. Applied Physics Reviews **2014**, 1, 011304.
- (74) Cowley, A. M.; Sze, S. M. Surface states and barrier height of metal-semiconductor systems. Journal of Applied Physics **1965**, 36, 3212–3220.
- (75) Bai, P.; Bazant, M. Z. Charge transfer kinetics at the solid-solid interface in porous electrodes. Nature Communications **2014**, 5, 1–7.
- (76) Marcus, R. A. Chemical and electrochemical electron-transfer theory. Annu. Rev. Phys. Chem. **1964**, 15, 155.
- (77) Marcus, R. A. On the Theory of Electron-Transfer Reactions. VI. Unified Treatment for Homogeneous and Electrode Reactions. The Journal of Chemical Physics **1965**, 43, 679–701.
- (78) Marcus, R. A.; Sutin, N. Electron transfers in chemistry and biology. Biochimica et Biophysica Acta **1985**, 811, 265–322.

- (79) Marcus, R. A. Electron Transfer Reactions in Chemistry: Theory and Experiment. Reviews of Modern Physics **1993**, 65, 599–610.
- (80) Chidsey, C. E. Free energy and temperature dependence of electron transfer at the metal-electrolyte interface. Science **1991**, 4996, 919–922.
- (81) Henstridge, M. C.; Laborda, E.; Rees, N. V.; Compton, R. G. Marcus-Hush-Chidsey theory of electron transfer applied to voltammetry: A review. Electrochimica Acta **2012**, 84, 12–20.
- (82) Laborda, E.; Henstridge, M. C.; Compton, R. G. Asymmetric Marcus theory: Application to electrode kinetics. Journal of Electroanalytical Chemistry **2012**, 667, 48–53.
- (83) Laborda, E.; Henstridge, M. C.; Batchelor-Mc Auley, C.; Compton, R. G. Asymmetric marcus–Hush theory for voltammetry. Chemical Society Reviews **2013**, 42, 4894–4905.
- (84) Zeng, Y.; Bai, P.; Smith, R. B.; Bazant, M. Z. Simple formula for asymmetric Marcus-Hush kinetics. Journal of Electroanalytical Chemistry **2015**, 748, 52–57.
- (85) Fletcher, S. The theory of electron transfer. Journal of Solid State Electrochemistry **2010**, 14, 705–739.
- (86) Fraggedakis, D.; McEldrew, M.; Smith, R. B.; Krishnan, Y.; Zhang, Y.; Bai, P.; Chueh, W. C.; Shao-Horn, Y.; Bazant, M. Z. Theory of coupled ion-electron transfer kinetics. Electrochimica Acta **2020**, 367, 137432.
- (87) Lien, C. D.; So, F. C.; Nicolet, M. A. An Improved Forward I-V Method For Nonideal Schottky Diodes With High Series Resistance. IEEE Transactions on Electron Devices **1984**, 31, 1502–1503.
- (88) Aubry, V.; Meyer, F. Schottky diodes with high series resistance: Limitations of forward I-V methods. Journal of Applied Physics **1994**, 76, 7973–7984.

- (89) Takami, N.; Hoshina, K.; Inagaki, H. Lithium Diffusion in  $\text{Li}_4/3\text{Ti}_5/3\text{O}_4$  Particles during Insertion and Extraction. Journal of The Electrochemical Society **2011**, 158, A725.
- (90) Wagemaker, M.; Van Eck, E. R.; Kentgens, A. P.; Mulder, F. M. Li-ion diffusion in the equilibrium nanomorphology of spinel  $\text{Li}_{4+x}\text{Ti}_5\text{O}_{12}$ . Journal of Physical Chemistry B **2009**, 113, 224–230.
- (91) Prezioso, M.; Merrih-Bayat, F.; Hoskins, B. D.; Adam, G. C.; Likharev, K. K.; Strukov, D. B. Training and operation of an integrated neuromorphic network based on metal-oxide memristors. Nature **2015**, 521, 61–64.
- (92) Malik, R.; Burch, D.; Bazant, M.; Ceder, G. Particle size dependence of the ionic diffusivity. Nano Letters **2010**, 10, 4123–4127.
- (93) Li, Y.; Liang, Y.; Robles Hernandez, F. C.; Deog Yoo, H.; An, Q.; Yao, Y. Enhancing sodium-ion battery performance with interlayer-expanded  $\text{MoS}_2$ -PEO nanocomposites. Nano Energy **2015**, 15, 453–461.
- (94) Hu, Z.; Liu, Q.; Sun, W.; Li, W.; Tao, Z.; Chou, S. L.; Chen, J.; Dou, S. X.  $\text{MoS}_2$  with an intercalation reaction as a long-life anode material for lithium ion batteries. Inorganic Chemistry Frontiers **2016**, 3, 532–535.
- (95) Santa-Ana, M. A.; Sanchez, V.; Gonzalez, G. Temperature effects on the diffusion of lithium in  $\text{MoS}_2$ . Electrochimica Acta **1995**, 40, 1773–1775.
- (96) Park, M.; Zhang, X.; Chung, M.; Less, G. B.; Sastry, A. M. A review of conduction phenomena in Li-ion batteries. Journal of Power Sources **2010**, 195, 7904–7929.
- (97) Li, Y.; Lu, Y.; Adelhelm, P.; Titirici, M. M.; Hu, Y. S. Intercalation chemistry of graphite: Alkali metal ions and beyond. Chemical Society Reviews **2019**, 48, 4655–4687.

- (98) Kühne, M.; Paolucci, F.; Popovic, J.; Ostrovsky, P. M.; Maier, J.; Smet, J. H. Ultrafast lithium diffusion in bilayer graphene. Nature Nanotechnology **2017**, 12, 895–900.
- (99) Gránásy, L.; Pusztai, T.; Saylor, D.; Warren, J. A. Phase field theory of heterogeneous crystal nucleation. Physical Review Letters **2007**, 98, 1–4.

## Graphic Abstract

